Marine and Petroleum Geology 158 (2023) 106569

Contents lists available at ScienceDirect

Marine and Petroleum Geology

journal homepage: www.elsevier.com/locate/marpetgeo

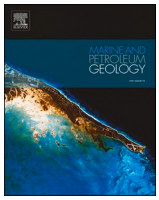

Quantification of mixed hydrate and free gas concentrations by the joint integration of velocity and conductivity information

Konstantin Reeck [a,*], Marion Jegen [a], Tim Freudenthal [b], Judith Elger [a], Sebastian Hölz [a], Christian Deusner [a], Klaus Wallmann [a], Saulwood Lin [c], Wu-Cheng Chi [d], Gerhard Bohrmann [b], Christian Berndt [a]

[a] GEOMAR Helmholtz Centre for Ocean Research Kiel, Wischhofstr. 1-3, 24148, Kiel, Germany
[b] MARUM Center for Marine Environmental Sciences and Faculty of Geosciences, University of Bremen, Leobener Str. 8, 28359, Bremen, Germany
[c] Institute of Oceanography, National Taiwan University, No. 1 Sec. 4, Roosevelt Rd., Taipei, Taiwan
[d] Institute of Earth Sciences, Academia Sinica, 128, Sec. 2, Academia Road, Nangang, Taipei, Taiwan

ARTICLE INFO

Keywords:
Gas hydrate
Free gas
Taiwan
Geophysics
Effective medium modelling
Joint inversion
Data science
Rock physics

ABSTRACT

Quantification of gas hydrates in marine sediments is crucial for understanding gas hydrate systems. By empirical relationships or effective medium modelling, gas hydrate concentrations can be derived from velocity and/or conductivity logs. However, these approaches do not take the co-occurrence of free gas and gas hydrate into account leading to large uncertainties in the calculated free gas and gas hydrate concentrations. To overcome this issue we adopt a joint elastic and electric self-consistent/differential effective medium model as the basis for a new joint inversion scheme that distinguishes between both phases. We apply this scheme to p-wave velocity and electric induction data measured by downhole-logging of boreholes at Formosa Ridge off Taiwan - a known hydrate province with an active gas conduit. Gaussian Mixture Modeling separates the background signal of the host medium from anomalies and allows to determine a background porosity as a probability density function of depth. We use this derived porosity to jointly invert electrical conductivity and velocity data for hydrate and free gas concentrations. At Formosa Ridge, we find two resistive anomalies, one in the shallow and another in the deep part of the borehole. Only the deep anomaly in conductivity coincides with a high-velocity anomaly. This is consistent with ~30% hydrate with ~1% free gas concentration. For the shallow anomaly, increased velocities due to hydrate concentrations of ~15% are compensated by a decrease in velocity due to ~1% of free gas. The method reconciles the different sensitivities of the two data types and yields hydrate and free gas concentrations that are largely consistent with geochemically derived values.

1. Introduction

Gas hydrates are solid, ice-like clathrates formed by a dense cluster of guest molecules trapped in water crystal cages, which form within low-temperature and high-pressure conditions that define the gas hydrate stability zone (GHSZ). Different types of gas molecules may occupy the cage structure but methane is the most common in naturally occurring hydrates (Bohrmann and Torres, 2006). The availability of fresh water in combination with free or dissolved gas from biogenic or thermogenic sources leads to the formation of gas hydrates whenever pressure and temperature conditions are favorable, including marine settings, inland lakes, and permafrost regions on land (Kvenvolden and McMenamin, 1980; Waite and Spangenberg, 2013). As 1 m^3 of methane hydrate carries over 160 m^3 of methane at standard pressure and temperature conditions, hydrates constitute a gigantic reservoir of carbon close to the Earth's surface and represent an important constituent of the global carbon cycle and a potential future energy source (Edwards, 1997; Dickens, 2003; Ruppel and Waite, 2020). On the other hand, the dissociation of methane hydrates poses natural hazards as a) the dissolution of present methane hydrates decreases sediment slope stability, and b) the release of methane gas, which is a potent greenhouse gas, would add to global warming if it reaches the atmosphere (Sloan, 1998).

* Corresponding author.
E-mail addresses: kreeck@geomar.de (K. Reeck), mjegen@geomar.de (M. Jegen), freuden@marum.de (T. Freudenthal), jelger@geomar.de (J. Elger), shoelz@geomar.de (S. Hölz), cdeusner@geomar.de (C. Deusner), kwallmann@geomar.de (K. Wallmann), swlin@ntu.edu.tw (S. Lin), wchi@sinica.edu.tw (W.-C. Chi), gbohrmann@marum.de (G. Bohrmann), cberndt@geomar.de (C. Berndt).

https://doi.org/10.1016/j.marpetgeo.2023.106569
Received 30 May 2023; Received in revised form 30 September 2023; Accepted 25 October 2023
Available online 26 October 2023
0264-8172/© 2023 Published by Elsevier Ltd.

The quantification of hydrates is key in methane hydrate research and includes the evaluation of the spatial and temporal distribution and saturation within the seafloor. Therefore, the occurrence, formation, dissociation, and mobilization of gas hydrates in sediments have been a topic of ongoing research for nearly 50 years and remain of high scientific and economic interest.

Seismic indicators for hydrate occurrences are found by an increase in compressional p-wave velocity (vp) over the background formation, whereas gas-bearing structures are marked by a decrease in vp. The base of the gas hydrate stability zone (BGHS) is the transect of the temperature profile with the phase boundary of the hydrate system. The geothermal gradient within the seafloor raises the temperature with depth beyond the favorable temperature/pressure conditions for gas hydrate formation. The transitional zone is marked by the shift from stable gas hydrates above to the occurrence of free gas below. The associated change from hydrate to gas-filled pores represents a drop in acoustic impedance which is marked by a high-amplitude negative-polarity seismic reflection, called the bottom simulating reflector (BSR). A typical approach to estimate average hydrate saturations is based on the observed increased vp in relation to an observed or assumed background sediment velocity, conveniently by empirical modeling (Lee et al., 1996). More sophisticated approaches combine geophysical datasets by including shear wave seismic velocities and electrical conductivity (Bünz and Mienert, 2004, Lee and Collett, 2005). Hereby, hydrate saturations from s-wave velocity analysis are less affected by co-occurring gas. Especially electromagnetics are considered very suitable to complement the widely available seismic datasets since the presence of hydrates or gas causes a marked resistive anomaly in the otherwise conductive host media (Edwards, 1997). Saturation levels can be derived from the application of Archie's Law (Archie, 1942). However, some circumstances prevent the formation of gas hydrates within the GHSZ: unavailability of fresh porewater, the presence of high saline porewater, or the local dissociation of hydrate by migrating warm fluids may lead to the co-occurrence of free gas and gas hydrates. Evidence of such processes beneath the seafloor are cold seeps, where fluids containing gas are expelled from the seafloor, leading to the formation of authigenic carbonates (Peckmann et al., 2001). Fluid and gas migration within the sediments are also evident in reflection seismic data which map seismic chimney structures of seep sites and gas horizons within the hydrate stability zone (Fig. 1b). The co-occurrence of hydrates and free gas complicates how we quantify gas hydrates since they might lead to false estimates derived from geophysical datasets by conventional methods. The additional free gas reduces vp and therefore the hydrate saturation estimates based on acoustic methods. At the same time, free gas will decrease the overall conductivity exceeding the calculated values based on present hydrates alone. Consequentially, the identification of the free gas is required to correctly differentiate and quantify the hydrate content. Our approach meets this requirement by the joint integration of electrical conductivity and seismic velocity data. The method improves overall gas hydrate estimates and may allow for a better constraint on formation and dissociation processes by complementary, geophysical datasets.

To estimate free gas and hydrate content, we require a connection between microscopic parameters, including the constituent fractions (i.e. concentration of sediment matrix, pore fluid, free gas/gas hydrate) and their elastic and electric properties with measured, geophysical quantities of a representative medium. Either empirical relations or physical, effective medium models provide this connection. For electric properties, the empirically-derived Archie's Law is commonly applied to calculate either porosities or saturation levels from conductivity data. However, since it has been parameterized based on investigations of sandy sediments where the rock matrix is very resistive, its application to clay-rich marine sediments requires additional, not well-determined corrections (Jackson et al., 1978; Glover et al., 2000). Effective medium models for electric properties exist but are not commonly used. For elastic parameters, empirical relations like Wyllie's time-averaging equation, Wood's averaging equation, or their weighted average are used to calculate bulk seismic velocities from the single constituents' velocities in a composite (Wood, 1941; Wyllie et al., 1956; Lee et al., 1996). However, more sophisticated, physical effective medium models are well established, including approaches by Dvorkin and Nur (1996) and the combination of self-consistent approximations and differential effective medium models (SCA-DEM) based on the work of Cleary et al. (1980), Berryman (1980, 1995), Hornby et al. (1994) and Sheng (1990, 1991). Both approaches have been successfully applied to invert gas hydrate saturations from vp information. Even though the combination of conductivity and velocity information is very advantageous for many applications (Ellis, 2008), joint elastic/electric effective medium models have rarely been used to exploit the complementary sensitivities. Han et al. (2011) applied the combination of a joint electric/elastic SCA-DEM model to improve the joint inversion of seismic and marine controlled-source electromagnetic data for reservoir sandstones. On this basis, Attias et al. (2020) applied the same approach to estimate hydrate saturation by integrating vp and electrical conductivity in hydrate-bearing clay sediments.

The main objective of this paper is to determine free gas as well as hydrate saturations in sediments by expanding the previous approaches of hydrate quantification by including the additional free gas phase. To meet this objective, we exploit the complementary changes in vp and conductivity data for free gas/gas hydrate mixtures using SCA-DEM effective medium modeling. To address uncertainties in the resulting hydrate/gas quantification, we explore the entire solution space to identify data-compatible ranges of hydrate/free gas saturations. We showcase our approach and its abilities using MeBo drilling data on the Formosa Ridge in the South Chinese Sea southwest off Taiwan from 2018 (Bohrmann et al., 2019, 2023). This area has been studied by Berndt et al. (2019) to investigate the occurrence, formation, and mobility of gas hydrates in its sedimentary setting based on a combined seismic and electromagnetic field data set. The MeBo drill hole intercepts an active seep site and chimney structure identified by the field data. The borehole data includes downhole gamma ray, vp, and conductivity logs as well as core-based lithological and geochemical data, which can be used as independent validation data, The MeBo dataset therefore provides the unique opportunity to develop a joint electric and elastic model to re-calculate gas hydrate saturations by including the additional free gas phase from the geophysical data and to compare them to the qualitative inferences that have been made earlier (Berndt et al., 2019).

1.1. Geological setting, drilling, and core data

Formosa Ridge is a sedimentary ridge located on the passive margin in the northern part of the South Chinese Sea southwest off Taiwan. The northwest-trending ridge with approximately 30 km length and 5 km width is formed by two, up to 700 m deep canyon incisions leading to steep slope angles of around 30°. Water depths vary from 1088 m along the summit in the north to 1125 m at the southern summit (Hsu et al., 2018). The stratigraphy of the northern and southern parts of Formosa Ridge is dominated by refilled canyons and contourites respectively (Berndt et al., 2019). The refilled canyons are indicated by several erosional unconformities with horizontally layered fillings. The southern part lacks these unconformities and shows sediment waves with undulating thicknesses and higher reflections at exposed areas indicating the formation of contourites. Seismic investigations show a widespread and almost continuous BSR for most of the region. The presence of a double BSR hints towards a dynamic gas hydrate stability field in the past (Berndt et al., 2014). This interpretation is supported by shoaling of the BSR towards the canyon incision in the north of Formosa Ridge. Beneath the southern summit of Formosa Ridge, a chimney structure cross-cuts the up-bending BSR and terminates in a gas seep at the seafloor (Fig. 1b). This site is the only one known to be active in this region (Feng and Chen, 2015). Ocean bottom seismometer-derived and

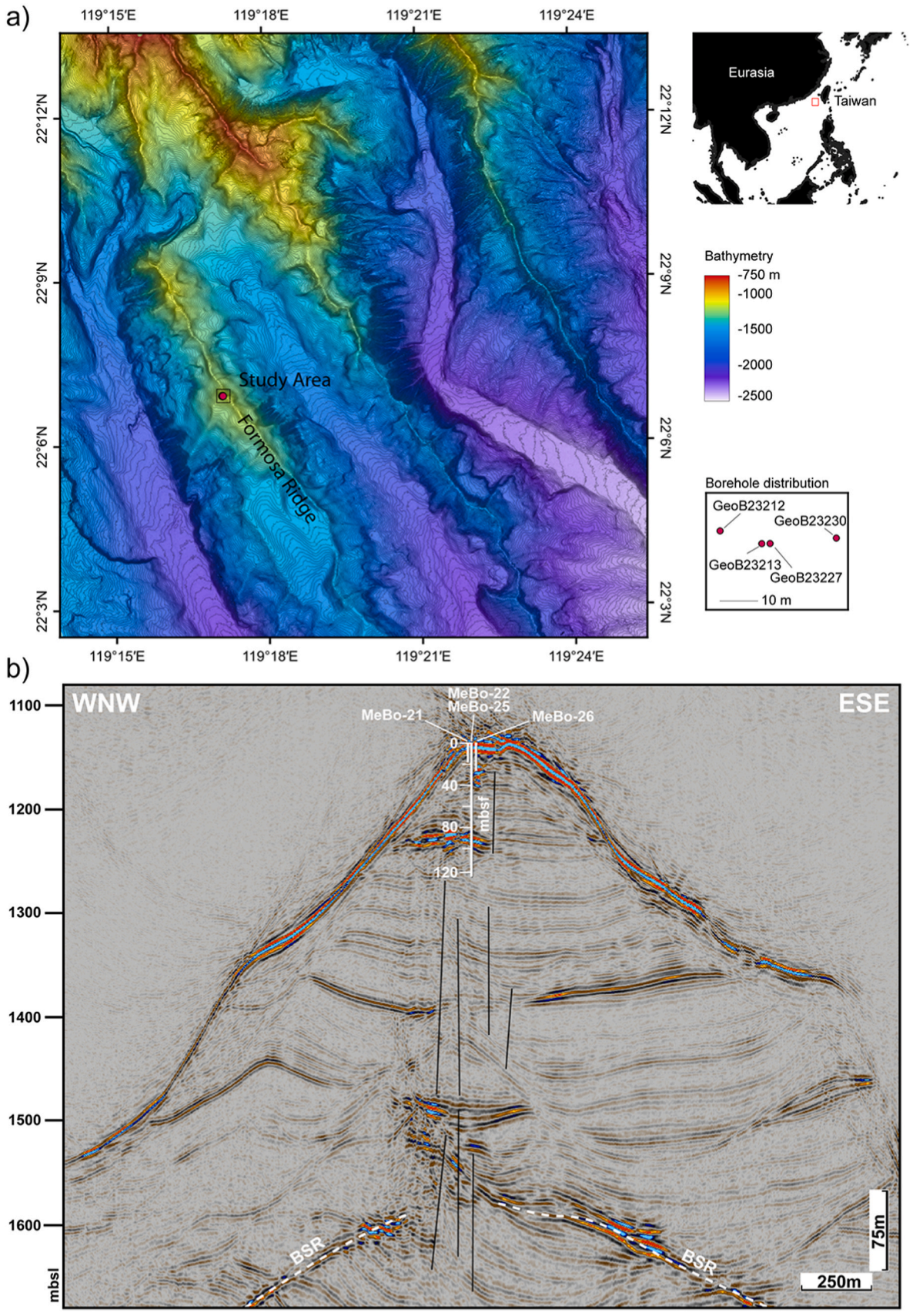

Fig. 1. a) Overview of Formosa Ridge and distribution of boreholes (see bottom right map for details) of GeoB23212 (MeBo21), GeoB23213 (MeBo22), GeoB23227 (MeBo25), and GeoB23230 (MeBo 26). MeBo22 and MeBo25 comprise the joint data set of p-wave velocity and electrical conductivity used for this study. b) Distribution of boreholes in the seismic section with indicated bottom simulating reflector (BSR, dashed white line) and identified faults that indicate the active seep structure. Identified, vertical faults are indicated as black lines.

prestack depth migration-derived p-wave velocities of up to 1850 m/s at the depth of the BSR (Berndt et al., 2019) indicate relatively low hydrate saturations of up to 10 % of the pore space. This is supported by concurrent low apparent resistivities of about 3 Ωm from CSEM data (Berndt et al., 2019). However, this saturation is poorly constrained due to the lack of borehole data at the time and the limited spatial resolution of the geophysical methods. The CSEM dataset indicates increased apparent resistivities for the chimney structure. Yet the dataset has not been inverted to a quantitative resistivity model but is restricted to the common midpoints of data conversion which results in a poor delineation of this feature. The gas rising through Formosa Ridge is predominantly formed by microbial breakdown of organic matter (Bohrmann et al., 2023).

The drilling at Formosa Ridge targeted the southern summit in direct proximity to the seismically imaged chimney and the cold seep site (Bohrmann et al., 2019): MeBo22/GeoB23213-1, equipped with a spectral gamma ray (SGR) tool and a memory acoustic tool (MAT), and MeBo25/GeoB23227-1, equipped with the SGR and a dual induction (DI) tool, were drilled within 5 m next to each other (Freudenthal, 2020a, b, c, d). The MAT measures p-wave velocities by transmitting acoustic pulses that are refracted along the well's wall and recorded by two individual receivers at 90 and 100 cm distance below the transmitter. The p-wave arrival times are analyzed and the difference in runtime between both receivers is characteristic for the velocity of the interval between them. Thus, the vertical resolution is 10 cm, with a depth of investigation of less than 1 m. The DI tool consists of transmitting coils as magnetic sources with operating frequencies of 50 kHz and 100 kHz. The secondary fields of the induced currents in the surrounding formation are recorded as 180° out-of-phase currents by two receiver coils. The different frequencies correspond to deep (1.3 m, 50 kHz) and shallow (0.65 m, 100 kHz) depths of investigation, with vertical resolutions of 1.3 and 0.65 m respectively. The SGR tool counts and measures the energy spectrum of light impulses that are generated by the scintillation of a cesium iodide crystal. The spectra are characteristic to the naturally occurring gamma ray emitters potassium, uranium, and thorium present in the surrounding formation. The signal may therefore indicate formation changes of sediments by the change in K, U, and Th concentration (Ellis and Singer, 2007). The logging data are acquired after the drilling process during the retrieval of the drill string (logging while tripping, Freudenthal and Wefer, 2013). Dissolved chloride concentrations were determined for both cores at various depths from porewater samples onboard the vessel by argentometric titration with 0.1 M AgNO3 and additionally by ion chromatography (Bohrmann et al., 2019, 2023, Lin and Bohrmann, 2022). Hydrate saturations were converted by the equation of Ussler and Paull (2001).

Due to the proximity of the first two boreholes, we assume that data from MeBo 22 and MeBo 25 can be viewed as concurrent data sets. MeBo 25 drilled down to 126.4 mbsf while MeBo 22 reached 109 mbsf, restricting the combined dataset to their common depths. Authigenic carbonates were encountered in the first meters before passing through an interval with visually confirmed gas release at 20–30 mbsf (Bohrmann et al., 2019). Several layers of seep carbonates were drilled between 84 and 94 mbsf before drilling into hydrate layers. Background host sediments are largely homogeneous clay (Fig. 6i). Porewater analyses provide an independent calibration for our derived hydrate estimates by detecting negative chloride anomalies due to dissolved gas hydrate in the cores. Hydrate dissolution is identified by negative chloride anomalies and described by lithological indicators like the mousse to soupy sediment structure of fresh-water clay mixtures (Bohrmann et al., 2023). The calculated values from the porewater samples suggest hydrate saturations of up to 40 % of the pore space in the lowest part of the core. However, no solid hydrate was recovered from the core material aboard. Bohrmann et al. (2023) relate this to the occurrence of hydrate as fine, disseminated crystals or thin veins that decompose while recovering the core from the GHSZ. MeBo 26/GeoB23213-1 was drilled about 15 m further west but was abandoned due to a visually observed, heavy gas release when it reached 23 m below seafloor (mbsf).

Authigenic carbonates at 90 mbsf are likely formed at the seafloor above the chimney structure by the already active seep site before and during the evolution of the ridge. Kunath et al. (2022) assign a major role to these layers, as they accumulate gas beneath and increase pore pressure until hydraulic fracturing leads to an episodic opening of vertical fracture networks and the upward migration of free gas. They interpret the presence of two bright spots as currently ascending gas fronts at 220 and 340 mbsf, indicating the system to be episodically active. While the upper pathways are not completely understood and may be more complex than just vertically aligned, the lower fracture network evolving from the up-bending BSR is likely to be stable since the formation of the ridge.

2. Methods

Determining simultaneously gas hydrate and free gas concentrations requires a robust estimate of sediment porosity. We use measured vp and σ values in borehole intervals devoid of gas hydrate and free gas for baseline calibration and porosity calculation. To test whether these background values can objectively be differentiated from anomalies, we apply Gaussian Mixture Modeling (GMM) as clustering method to the measured parameters σ, vp, and SGR. Based on the a-priori knowledge from the sediment core description we assume that the sediments comprise a combination of five major constituents: gas hydrates, free gas, pore-water, carbonates, and the host medium (clay). The second step is to couple rock physics with geophysics, requiring either an empirical relationship or a more sophisticated physical model. In either case, the microscopic electric and elastic properties of the single constituent matrix- and pore-filling fractions are linked to the geophysically measured, macroscopic quantities of a composite defined by its bulk conductivity and bulk velocity. The choice of models mainly depends on the availability of data and a-priori knowledge, including properties of the occurring formations, but also on technical limitations like computing capabilities.

We initially developed a proof of concept to derive gas hydrate and free gas concentrations from combined seismic and electromagnetic data by an empirical model. For elastics (acoustic data), averaging equations like Wyllie's time averaging equation (Wyllie et al., 1956) or Wood's equation (Wood, 1941) are commonly used. For both cases the inverse of the velocity (Wyllie) or the inverse of the density-velocity product (Wood) is summed by the fraction of the occurring phases. These empirical formulations relate to consolidated rocks (Wyllie) and suspension-like unconsolidated sediments with high porosity and water content (Wood), which forms an upper and lower limit respectively (Lee et al., 1996). Lee et al. (1996) combine both equations with an additional weighting and lithification factor to fit them to measured datasets. Given the assumption that the fluid saturated pore-space controls the electric properties in an otherwise perfectly insulating matrix, the most popular option to determine the bulk conductivity (C_b) is certainly Archie's Law (Archie, 1942)

$$C_b = \frac{1}{a} C_w \phi^m S_w^n. \quad (1)$$

C_w hereby denotes the conductivity of the pore fluid that saturates (S_w) the porespace (ϕ). In the equation, gas hydrates may be implemented as a reduction in pore space saturation (Collett and Ladd, 2000). The tortuosity (a) and cementation (m) are empirical, formation related factors that are commonly used to fit measured data in absence of a reduced saturation. In an equal manner, the saturation exponent (n) can be used to model the influence of the resistive phase in the pore space on its conductivity. In a trivial approach, the elastic and electric equations can then be joined by using the porosity as common ground which needs to be determined from a background signal of p-wave velocity and conductivity. However, initial testing showed inconsistent results in the

derived porosities, indicating that the empirical relationships represent the geological setting of the study area insufficiently. This is likely due to Archie's Law not considering a conductive clay rock matrix as encountered on Formosa Ridge. Consequently, we adopt the combined self-consistent approximation/differential effective medium model (SCA-DEM) as a physical effective medium model (see section 2.2.1). By the joint methodology, the elastic and electric parts are treated equally, which allows a more congruent combination of elastic and electric data. In a statistical approach, we present the results as probability density functions.

2.1. Clustering by Gaussian Mixture Modeling

To separate background information from anomalies it is advantageous to use machine learning algorithms to objectively classify the available data, rather than to rely on subjective interpretations. Since we may not know all specific constituents and their mixing ratios, we use MATLAB's Gaussian Mixture Modeling (GMM), an unsupervised, soft clustering algorithm that requires only a given number of classes as a priori knowledge (MATLAB, 2021). GMM provides the probability of each data point belonging to all classes rather than an explicit assignment towards a specific class. The GMM algorithm fits the given number (K) of Gaussian distributions (classes), defined by their means (μ_k) and covariance matrix (Σ_k) to the dataset X of length Z in each of its dimensions D (Deisenroth et al., 2020). In our case, we use three dimensions, i.e. conductivity, vp, and spectral gamma ray as functions of depth (Z). The probability density p of a given data point x_z belonging to a k-th multivariate Gaussian distribution is defined by

$$p\,(x_z|\mu_k,\Sigma_k)=\frac{1}{\sqrt{(2\pi)^D det\,\Sigma}}exp\big(-0.5(x_z-\mu_k)^T\Sigma^{-1}(x_z-\mu_k)\big), \tag{2}$$

while the probability density P for all distributions is given by

$$P(x_z|\Theta)=\sum_{k=1}^{K}\alpha_k p_k(x_z|\theta_k\Big), \tag{3}$$

where α_k defines the mixing weights being $0 \le \alpha_k \le 1$ and $\sum_{k=1}^{K}\alpha_k = 1$. Θ is a parameter set consisting of weights (a_k) and parameter subsets (θ_k) for each of the k distributions with $\Theta = \{a_1, \ldots a_k, \theta_1, \ldots \theta_k\}$ and $\theta_k = \{\mu_1, \ldots \mu_k, \Sigma_1, \ldots, \Sigma_k\}$. The (negative) logarithmic likelihood of the dataset x in relation to the set of chosen distributions can then be defined as

$$-logL(X,\Theta)=-\sum_{z=1}^{Z}\log P(x_z|\Theta)=-\sum_{z=1}^{Z}\log\sum_{k=1}^{K}\alpha_k p_k(x_z|\theta_k) \tag{4}$$

To fit an initially guessed set of distributions to the dataset, we apply an expectation maximization algorithm to adjust the weights, means, and covariance matrices of the Gaussian distributions as such they reach the highest probability ("maximum likelihood") over all data points. Here a weighting matrix w of size Z x K is calculated where each assignment represents the probability of the z-th data point being generated by the k-th distribution:

$$w_{zk}=\frac{\alpha_k p_k(x_z|\theta_k)}{\sum_{j=1}^{K}\alpha_j p_j(x_z|\theta_j)}\ . \tag{5}$$

The result is positive-definite with the sums $\sum_{k=1}^{K} w_{zk} = 1$ and $N_k = \sum_{z=1}^{Z} w_{zk}$. In the maximization, we then use the weights to re-calculate new weights (α^*) means (μ^*) and covariance-matrices (Σ^*) for each distribution:

$$\alpha_k^*=\frac{N_k}{Z}, \tag{6}$$

$$\mu_k^*=\frac{\sum_{z=1}^{Z} w_{zk}x_z}{\sum_{z=1}^{Z} w_{zk}}, \tag{7}$$

$$\Sigma_k^*=\frac{1}{N_k}\sum_{z=1}^{Z} w_{zk}\left(x_z-\mu_k^*\right)\left(x_z-\mu_k^*\right)^T, \tag{8}$$

On this basis, we calculate new posterior probabilities by equation 3 and repeat all steps until the minimum negative logarithmic likelihood is reached. Since this approach requires a fixed number of classes (distributions) being fitted to the data, the optimal number of classes K needs to be evaluated. In a perfect case, the best fitting number of classes should represent every lithological class, as well as anomalies. In realistic scenarios, fuzziness is added due to gradual changes and measurement errors. For our data, we apply a procedure following the principle of Occam's Razor: classes are continuously added while a metric measures the quality of fit. This method is widely known as the "Elbow Method" to calculate the negative logarithmic likelihood of the expectation maximization algorithm for up to 20 classes. Naturally, the addition of classes increases the quality of fit until each data point is covered by its very own class. However, we find an optimum if the lowest number of classes achieves a sufficient fit, from which further addition of classes only leads to a non-substantial increase in fit. This point marks the characteristic bend in a cross plot of the neg. log. likelihood vs. number of classes (the "elbow"). The elbow method hereby directly connects to the GMM by using the derived likelihood but may be prone to a certain bias, based on non-unique bends in the curve. In this case we explore also the next-best solution to investigate the stability of our background signal. In the first step, we use the algorithm on a two-dimensional dataset containing only vp and conductivity information which would represent a common combined geophysical dataset. In the second step, we include spectral gamma ray information as a third dimension which represents stratigraphy information for a seismic dataset.

2.2. Rock physics

2.2.1. SCA-DEM

Following the approaches of Ellis (2008), Han et al. (2011), and Attias et al. (2020), we initially calculate the self-consistent elastic/-electric moduli (K_{SC}, G_{SC}, σ_{SC}) by Berryman's formulation for an N-phase composite (Berryman, 1980, 1995; Mavko et al., 2009). These equations determine the representative (self-consistent) properties of a mixture of single constituents, called composite. This is achieved through minimization of the sum of differences between the elastic moduli and electric conductivity of the i-th material (K_i, G_i, σ_i) and the self-consistent moduli/conductivity of the composite by their fraction (x_i)

$$\sum_{i=1}^{N} x_i(K_i-K_{SC})*P^i=0, \tag{9}$$

$$\sum_{i=1}^{N} x_i(G_i-G_{SC})*Q^i=0, \tag{10}$$

$$\sum_{i=1}^{N} x_i(\sigma_i-\sigma_{SC})*R^i=0. \tag{11}$$

P^i, Q^i, and R^i are geometric coefficients related to the aspect ratio of the grain shape of the i-th material (see Mavko et al., 2009). For the combined SCA-DEM approach, the fraction x_i is equal to the critical porosity φ_c (Ellis, 2008). At critical porosity the medium stays bi-connected, which means that the constituents form interpenetrating infinite networks. For the solid/fluid mixture, this implies that for porosities of $\phi < \varphi_c$ minerals are load bearing while for $\phi > \varphi_c$ a

suspension-like behavior is attributed by a load-bearing fluid. φ_c typically ranges between 40 and 60 % for the elastic formulation. Han et al. (2011) and Attias et al. (2020) used the same values for the critical porosity for electric and elastic SCA formulation. However, we do not see a clear indication why this necessarily has to be the case, considering that the bulk p-wave velocity depends on the property of the solid matrix and their connectivity, whereas the bulk conductivity depends on the property of the pore fluids and their connectivity. Thus, we allow different values of electric and elastic critical porosities within a particular sediment. Equations (9)–(11) can be solved by optimization as such that the self-consistent parameters are re-evaluated in an iterative process until the change from the previous iteration (j) falls below a defined error χ:

$$\chi = \left| K_{SC,j} - K_{SC,j+1} \right| \tag{12}$$

The start value for K_{SC}, G_{SC} and σ_{SC} need to be guessed. A reasonable estimate can be derived from the Voigt-Reuss-Hill's Average, as given exemplarily for the bulk modulus by equation 13. The start value for σ_{SC} can be provided by an estimated background conductivity which may be derived from Archie's Law.

$$K_{SC} = \frac{1}{2}\left(\sum_{i=1}^{N} x_i K_i + \left(\sum_{i=1}^{N} \frac{x_i}{K_i} \right)^{-1} \right). \tag{13}$$

After the computation of the composite parameters at the critical porosity, we use the differential effective medium approach (eq. 14–16). The retrieved SCA bulk and shear moduli of the composite function as starting points from which we calculate these properties in infinitesimal steps over all possible concentrations (Fig. 2b). In Fig. 2b this concentration x_2 corresponds to the porosity of the clay/water mixture.

$$\frac{dK^*}{dx} = \frac{(K_2 - K^*)P^{(*2)}(x)}{1-x}, \tag{14}$$

$$\frac{dG^*}{dx} = \frac{(G_2 - G^*)Q^{(*2)}(x)}{1-x}, \tag{15}$$

$$\frac{d\sigma^*}{dx} = \frac{(\sigma_2 - \sigma^*)R^{(*2)}(x)}{1-x}. \tag{16}$$

K_2, G_2, and σ_2 denote the elastic and electric moduli of the incrementally added inclusion. K*, G*, and σ* represent the effective, elastic, and electric moduli of the host material at the concentration x of the inclusion, with the initial startpoints $K^*(0) = K_{SCA}$, $G^*(0) = G_{SCA}$ and $\sigma^*(0) = \sigma_{SCA}$. P, Q, and R are the geometric coefficients between both phases. These ordinary differential equations can be solved with the Euler method or any other simple Runge-Kutta method. In our case, we modified the available and well-known RPH toolbox from Mukerji (2009) with MATLAB's lsqnonlin function for the SCA formulation and extended it to the electric part. From the DEM equations (eq. 14–16) it is noticeable, that only two constituents are handled at once. This implies that a multi-constituent sequence consists of several, stacked SCA-DEMs. In our case, we calculate the hydrate and free gas mixture with their relative concentrations first, before determining the resulting mixture within the pore space by including porewater. While the background medium at Formosa Ridge consists of clay, a mixed matrix including an additional solid phase, can be build up by an equal procedure. In the final step, both matrix and pore space constituents are mixed. The properties of the used constituents are given in Table 1. We have to denote that we use a low conductivity of 10^{-5} S/m for gas hydrate which is in accordance with values from Constable et al. (2020). The conductivity of free gas is chosen equally at 10^{-5} S/m for the reason that a perfect insulating phase would source numerical instabilities into the code. Due to the large conductivity contrast towards the matrix and pore

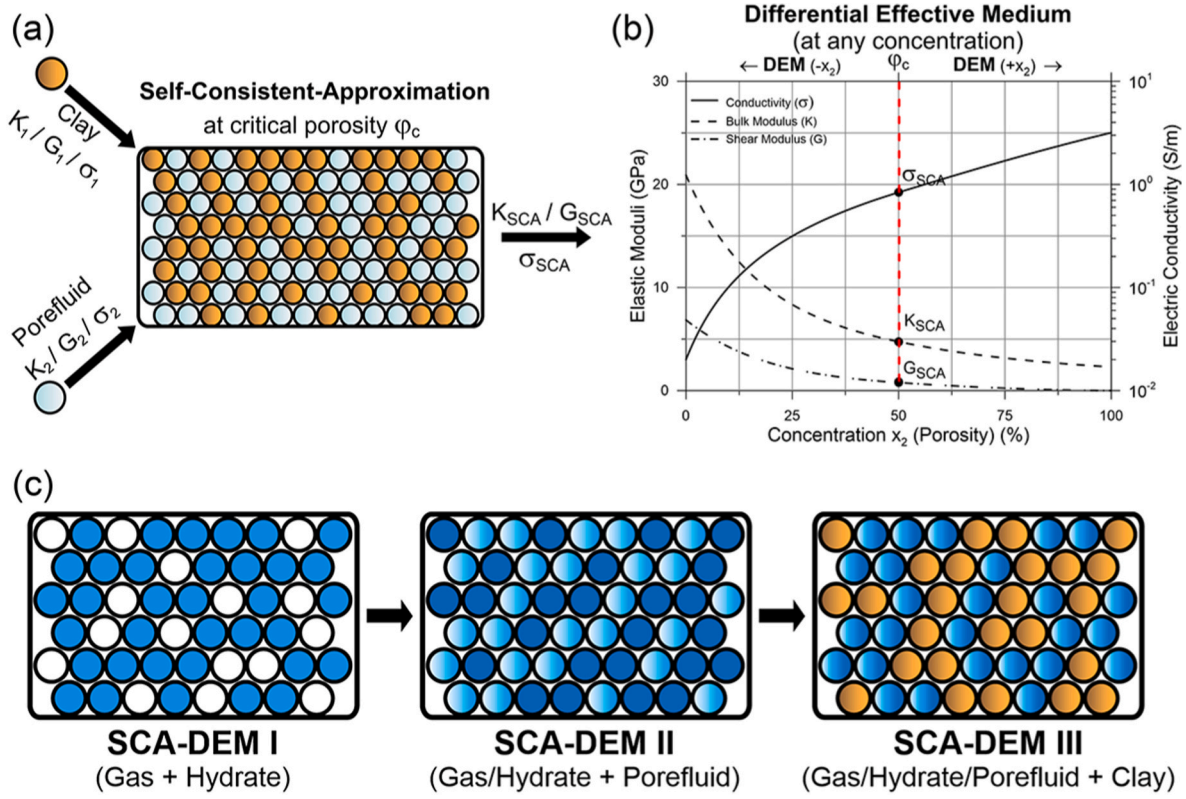

Fig. 2. Schematics for the (a) self-consistent approximation to calculate the self-consistent moduli at the critical porosity and (b) differential effective medium model to calculate a two-phase clay/porewater composite over the complete concentration range. The stacking of a multi-phase composite is shown in (c) for a free gas/hydrate/pore fluid mixture in the pore space with clay as matrix material.

Table 1
Material properties used for bulk modulus (K), shear Modulus (G), density (ρ), and conductivity (σ) of the constituents.

Constituent	K (GPa)	G (GPa)	ρ (g/cm^3)	σ (S/m)	Source
Clay	20.9	6.85	2.58	0.02	Helgerud et al. (1999)/ Han et al. (2011)
Porewater	2.29	0	1.025	3–3.5*	Han et al. (2011)/*measured
Gas Hydrate	7.9	3.3	0.9	10^{-5}*	Helgerud et al. (1999)/* Constable et al. (2020)
Free Gas	0.11*	0*	0.23*	10^{-5}	*Helgerud et al. (1999)

fluid, this is of no consequence for our result. Since the stacking sequence is fixed throughout the inversion, we have to decide whether the gas hydrate is located in the pore space or the matrix. In previous studies, the vast majority of authors described the hydrate phase as pore-space fillings for clayey to clay-dominated systems like Hydrate Ridge (Westbrook et al., 1994, Bohrmann et al., 1998, Pan et al., 2017, 2020), the Kirshna-Godavari Basin (Kumar et al., 2014, Panday and Sain, 2022), or the CNE03 pockmark offshore Norway (Attias et al., 2020). A nearby study located at sedimentary ridges on the same passive margin in the Shenhu area found the occurrence of gas hydrates to be disseminated in the pore space in the clay-dominated environment with saturations of up to 50 % of the pore space and a co-occurring gas phase (Zhang et al., 2007; Wu et al., 2011, Qin et al., 2020). On the other hand, the occurrence of hydrate in the pore space is debated since authors including Holland et al (2008) suggest that grain-displacing hydrate morphologies like veins or lenses may be the most common type for fine-grained sediments.

For our case, we don't have any direct evidence (e.g. pressure cores) for either of the hydrate configurations. Thus, we decided to implement hydrates in the stacking sequence as pore-fillings following most authors and the nearby study and chose to investigate the influence of a matrix-supporting type on our model and results additionally (section 2.2.3). Still, in contrast to grain displacing lenses, a vein type configuration isn't possible to model since this concept contradicts the idea of a representative, homogenized effective medium model of an incremental volume that is measured by geophysics. Given the decimeter resolution of the MAT and the even larger, volumetric footprint of the DI probe, it's improbable that thin vein type configurations would be resolvable with our methods other than by measuring an overall change of the volume's bulk properties.

2.2.2. Workflow

First, we develop the background model on basis of the background data points classified by the Gaussian mixture modeling (Fig. 3, left). We assume that the background model consists only of a clay matrix and porewater. For fixed values for the geometrical parameters in the SCA-DEM model, only the critical porosities ($\varphi_{c,VP}/\varphi_{c,\sigma}$) may vary. The critical porosities hereby control the elastic and electric porosities (ϕ_{VP}/ϕ_{σ}) since they provide the starting point of the DEM curves over all constituent saturations. The aim of the background model is therefore to provide information on the elastic and electric critical porosities as key parameters to fit the SCA-DEM model and to derive the most probable porosity distribution in the borehole. At this point, we join our model since the measurement-specific porosities ϕ_{VP} and ϕ_{σ} have to coincide which allows us to derive the overall porosity from valid combinations of $\varphi_{c,VP}$, and $\varphi_{c,\sigma}$ that meet this criterion. Porosities determined from the DEM curves over all possible concentrations that match the measured background data pairs ($VP_{bg,obs}$, $\sigma_{bg,obs}$), need to fall within specified error bounds, which we chose to be 3 %. All invalid combinations exceeding those bounds are discarded. This assumption is valid for a range of combinations of critical porosities within the allowed deviation. We therefore introduce input parameter distributions for the critical porosities as probability density estimates into our approach to avoid a restriction to single, fixed values. The applied error (3%) is not data-driven but relates to the fact that enough valid solutions are needed to build probability-density distributions. A higher error at a given input sample number directly relates to a wider distribution and less precision in the prediction of porosity and therefore hydrate and free gas concentrations. The critical porosity can be understood to be related to the underlying rock physics but also to the sensitivity and methodology of the measured vp and conductivity as elastic and electric parameters respectively: conductive measuring methods may lead to different resulting conductivities than inductive measurements. Thus, we treat the critical porosities as data-driven parameters that can be fitted to the observed data and which fall in specific ranges rather than to specific values. To exploit this characteristic, we chose Gaussian input distributions for the critical porosities that result in uncertainty estimates.

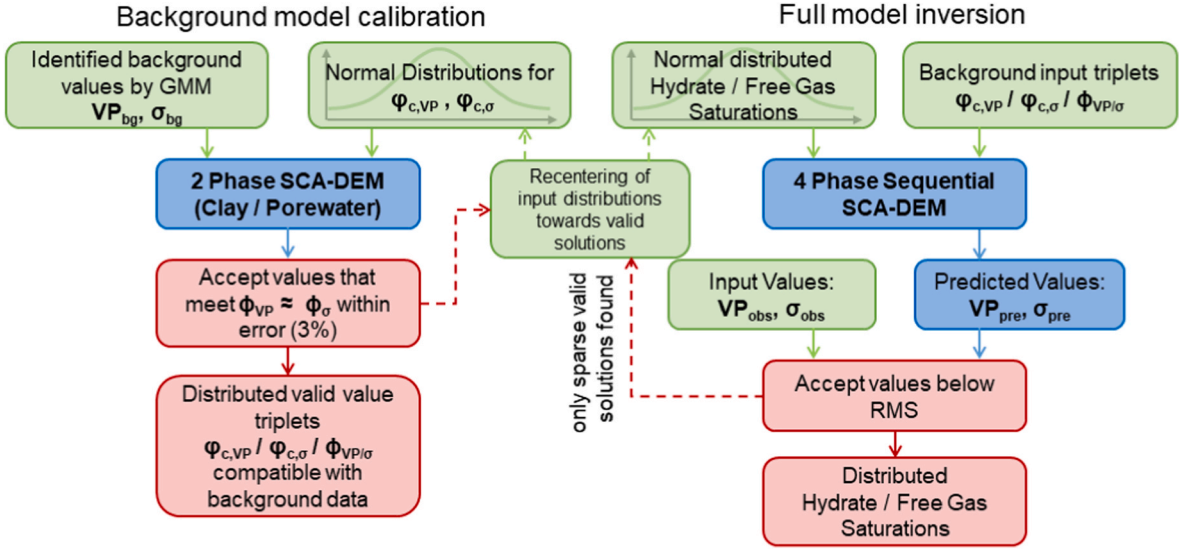

Fig. 3. Workflow diagrams for background model calibration (left), and full inversion routine (right). The background model calibration is required to determine the critical porosities by which the model is fitted to the observed background data, identified by the Gaussian Mixture Modeling. The determined valid value triplets, consisting of the two critical porosities and background porosity are then used to invert the complete dataset. The uncertainty measure is obtained by using normal-distributed input parameters.

Variations of grain aspect ratios also lead to variations in the vp vs. conductivity curves (Han et al., 2011), yet we chose to calibrate our background model based on the critical porosities and fix the aspect ratio to a constant value of 1 to avoid random ambiguities that would increase our workload unnecessarily. The initial distributions for the critical porosities have 10,000 value combinations with ranges between 0.4 and 0.6 for $\varphi_{c,VP}$, centered at 0.5 and 0.2–0.8 for $\varphi_{c,\sigma}$. , also centered at 0.5. If only a small number of fitting combinations is found, these distributions can be narrowed and re-centered towards the fitting distributions in a second cycle. With enough valid value pairs of $\varphi_{c,VP}/\varphi_{c,\sigma}/\phi_{\sigma/VP}$ for each depth point, we can use these as input distributions to invert for gas and hydrate saturations. For this step, we expand the input distributions by two additional dimensions containing hydrate and free gas saturation (Fig. 3, right). These distributions are positive definite as pore space fillings, meaning their absolute value is taken even though they are centered at zero and ranging between −1 and 1 for hydrate, and centered at zero, between −0.3 and 0.3 for gas, to account for a reasonable trade-off relationship. For each of the 10,000 four-dimensional inputs, the complete, four-phase sequential SCA-DEM is now calculated and evaluated against the observed vp_{obs}/σ_{obs} value pairs at each depth step. The calculation at each depth step is necessary as porewater conductivity, measured at the surface, is adjusted with depth based on a temperature profile, which was derived from heat flow measurements and the BSR depth after standard procedure (Grevemeyer and Villinger, 2000). The pore water conductivity therefore ranges from 3.0 to 3.5 S/m (Table 1). Theoretically salinity variations could have a similar effect but are proven to be very low by the negligible Cl-variations from the core, in absence of the anomalies of the dissolved gas hydrate (Bohrmann et al., 2023). Due to the low impact in the range of the applied 1% error, we do not correct the vp signal for temperature. For the final evaluation, only solutions with a combined RMS below 2 are accepted under the assumption of a 1% error for the measured vp and a 5% error for the measured conductivity. These errors do not only represent the data error in measurement, but also the trade-off in sensitivity between both methods to given increase in hydrate or free gas. The influence of the single and combined error as a measure of uncertainty is visible in Fig. 4.

2.2.3. *Validation of SCA-DEM model calculations*

After verifying our model with vp vs. porosity and conductivity vs. porosity curves for different critical porosities provided by Han et al. (2011), we establish a proof of concept to check if the co-occurrence of hydrate and free gas can be determined from a combination of vp and conductivity data. We generate synthetic, forward-calculated conductivity and vp pairs based on the SCA-DEM model, assuming a 50 % porosity clay host sediment with a concurrent 20 % gas hydrate and 3 %

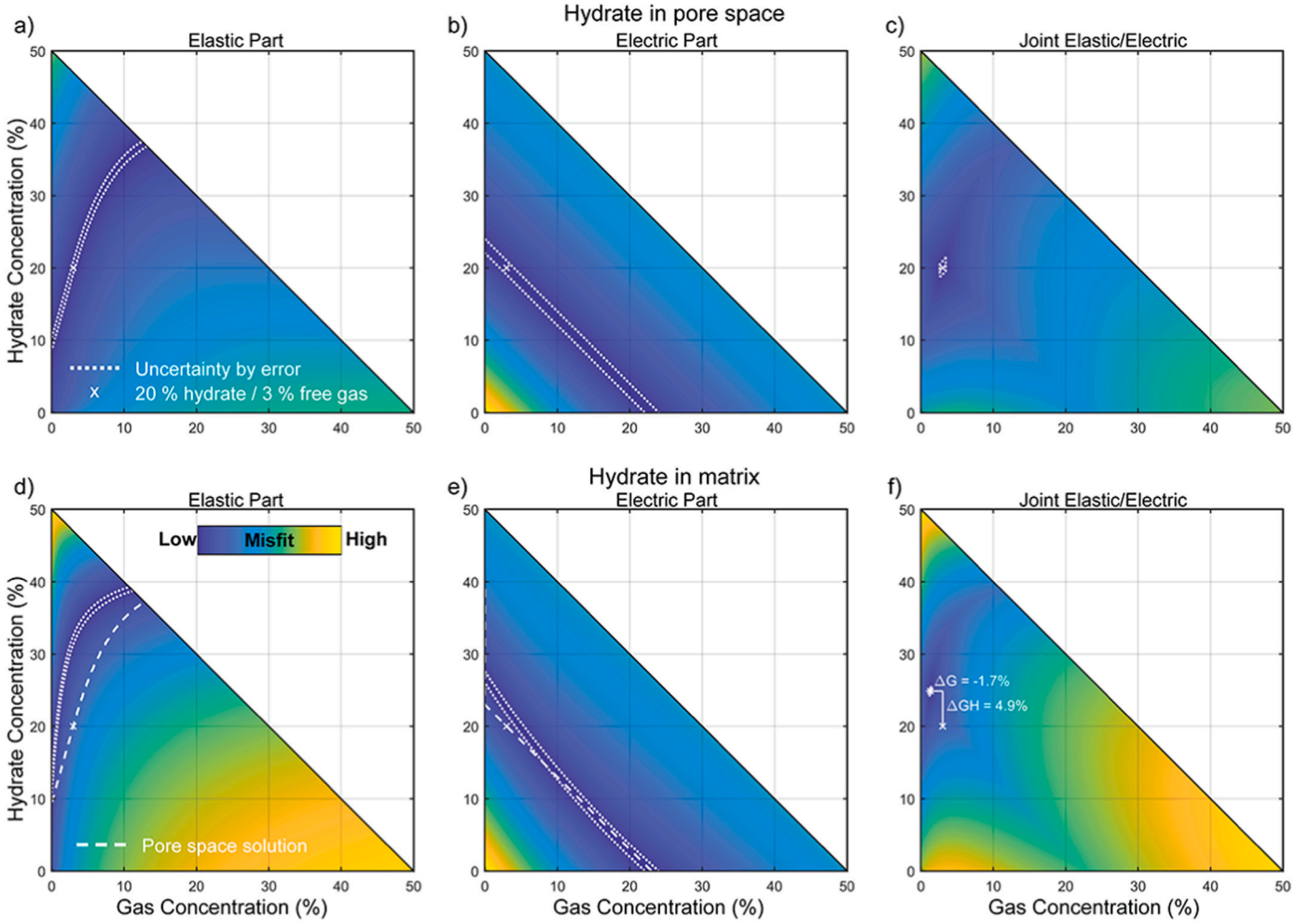

Fig. 4. Sensitivity diagrams of an (a, d) elastic-only model, (b, e) electric-only model, and (c, f) joint elastic/electric model for hydrate in pore space (a–c) and matrix-supporting mode with indicated misfit minima from pore-space configuration as dashed lines (d–f), The results are displayed as misfits towards a predefined hydrate and gas concentration of 20 %/3 % at a fixed porosity of 50 %. The correct solution can be only determined by a joint elastic/electric approach, while a matrix-supporting hydrate occurrence leads to higher hydrate (4.9%) and lower free gas (−1.7%) saturations (f). Here the minimum in misfit is indicated with a point marker for the matrix-supporting configuration, and as cross marker for the pore-space configuration. Further we indicate the uncertainty in the determination of the correct solutions by the applied errors (1% for vp and 5% for conductivity) by dotted lines.

free gas concentration. We calculate vp and conductivity values by single elastic (Fig. 4a, d) and single electric (Fig. 4b, e) methodologies as well as joint vp/conductivity pairs (Fig. 4c, f) for all possible combinations of hydrate and free gas concentrations. We then determine a misfit between vp and conductivity values for all concentration combinations up to the complete filling of the pore space (50% concentration at 50% porosity), and the synthetic values of the specified 20 % hydrate/3 % gas model. The results in Fig. 4 showcase the different sensitivities to free gas and gas hydrate concentrations of the single and joint SCA-DEM models: for the elastic model, we observe a trade-off sensitivity. An increase in vp is proportional to hydrate saturation, yet an increasing free gas saturation decreases vp. Thus any gas hydrate saturation can be balanced by a particular gas concentration to yield the synthetic vp values of our model (Fig. 4a). We find a monotonically increasing function of minimum misfit of hydrate saturation as a function of free gas saturation as likely solutions with no clear indication of the true individual concentration levels. For the synthetic electrical conductivity, the minimum misfit is a monotonically decreasing function of hydrate saturation as a function of gas saturation, since hydrates and free gas are both resistors (Fig. 4b). Again, there is no clear indication of the true hydrate and free gas saturation value. In our proposed joint approach, where we require that both, synthetic conductivity and vp, data are met, possible solutions of concurrent gas and hydrate saturations converge to an overall minimum (Fig. 4c) at the chosen gas/gas hydrate saturation, illustrating the increased sensitivity and possibility to identify the correct gas and gas hydrate saturations.

To investigate the effect of hydrate occurrence as matrix-supporting instead of the pore space disseminated configuration, we change the

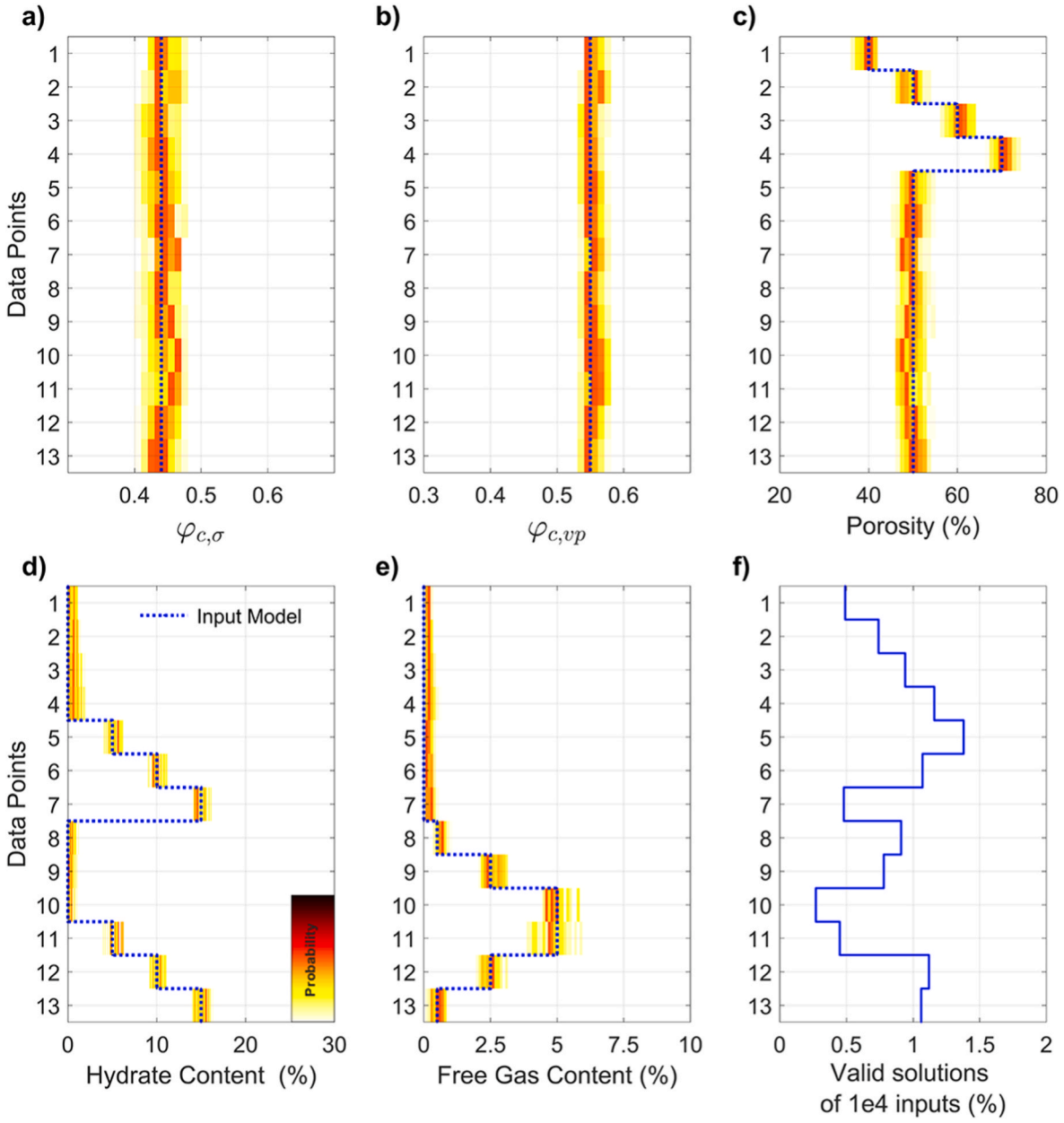

Fig. 5. Benchmark test for 13 different model parameter combinations (data points) of porosity (c), hydrate (d), and free gas (e) saturations. The critical porosities remain fixed for both the electric (a) and elastic (b) parts of the input model but are freely determined during the background calibration. The blue, dashed lines indicate the synthetic 'true' model parameters while possible valid solutions are shown as histograms of the solution density. A smaller amount of actual valid solutions from the 10,000 input values (f) lead to scattering in the solution density (e.g. data points 10 and 11). In these cases, a re-centering of the input distribution towards the possible solutions would help to enhance the resolution.

SCA-DEM model to a different stacking sequence. As discussed in section 2.2.1 this sequence consists of a clay/hydrate mixture for the matrix phase and a free gas/porewater mixture for the pore space phase, ultimately mixing them in the last step. However, hydrate is not displacing clay in the matrix but reducing the effective pore space to assure comparability between models. The difference in predicted electrical conductivity and vp estimates can be deduced from Fig. 4 (d – f). Resulting minimum misfit velocities and conductivities deviate slightly from our chosen pore space model, especially for hydrate saturations between 20 and 40 % of the pore space. The velocities are slightly lower while the conductivities are higher for the matrix-supporting hydrate type. Thus, if the hydrate saturation is matrix-supporting hydrate instead of, as assumed in the generation of the synthetic data, distributed in the pore space, a higher amount of hydrate saturation is required to explain a given high vp/low conductivity anomaly at low to medium saturation levels. Accordingly, a higher amount of free gas would be needed to balance anomalies.

2.2.4. Benchmark tests

Following the proof of concept, we benchmark the complete algorithm and workflow on the synthetic data set to check the robustness and uncertainty estimates of our solutions. For this task, we calculate forward solutions for vp and σ for constant $\varphi_{c,VP}/\varphi_{c,\sigma}$ values of a clay background medium for 13 data points with different combinations of porosity, hydrate, and free gas saturations (Fig. 5a-e, blue dashed line). We apply a random error of 1 % to these values. Following the workflow, we first estimate valid critical porosities combinations from the first four data points that represent the background medium to reconstruct the different porosities (see Fig. 3a). We then invert for combined gas hydrate and free gas concentrations for all steps. For any of the cases, we can conclude that the initially used saturations can be correctly retrieved, while the probability density functions have error ranges of about ±5 % of the original input values (Fig. 5c–e). This mostly relates to the uncertainty in the determination of the critical porosities. Due to the fact, that we use generalized input distributions centered at a value of 0.5 for the critical porosities and zero for hydrate/free gas saturations only a few valid solutions are found: of 10,000 input parameter combinations of the valid value triplets and hydrate/free gas saturations, only ≤100 combinations are valid solutions that can represent our synthetic data set (Fig. 5f). A re-centering of the input distributions towards the probable, retrieved valid solutions in the first parameter sweep would increase the number of solutions and result in smoother probability distributions of hydrate and gas concentrations in a second parameter sweep.

3. Results

3.1. Background determination by Gaussian Mixture Modeling

Based on the Gaussian Mixture Modeling (GMM) we distinguish several classes to characterize the borehole data (Fig. 6c–e) that are described by their multi-dimensional centroids and covariance matrices. These are especially useful to predict and interpolate missing data for a specific class like the host medium if necessary. In Fig. 6 we present the data as inverse conductivity (1/σ, resistivity) for better visibility in the cross plots. The elbow method identifies 4–6 classes as points of strongest bend for the combination of vp, resistivity, and SGR information (Fig. 6a). The identified minimal solution of four classes is defined by the drastically decrease in neg. log. likelihood and correlates well with the lithological information of the borehole (Fig. 6i): one class represents the homogeneous clay (background), one class represents the occurrence of carbonate nodules, and two classes represent the anomalies I and II as gas hydrate occurrences. Anomaly I is primarily defined by the distinct separation from anomaly II in the resistivity vs. SGR crossplot (Fig. 6c). The missing vp deviation leads to the complete vanishing of anomaly I in the vp vs. SGR crossplot while anomaly II is easily visible (Fig. 6d). Moussy textures in the lithology represent the deeper anomaly II in the core (Fig. 6i). In Fig. 6b the pseudo confusion matrix indicates the development of the initial four classes if two further classes, ac1 and ac2 would be added. This increased number of classes as maximum solution corresponds to the second part of the bend that we can identify from the elbow plot. The addition does not yield any statistical improvement in fits to our observations and rather splits the existing four classes into new redundant ones. This especially applies to upper anomaly I, which ranges from 15 mbsf to approximately 40 mbsf and relates to gas hydrates identified by chloride anomalies, but also for the class which relates to the occurrence of carbonate nodules at depths of 85–98 mbsf and a spike in vp at 72.5 mbsf corresponding to an ashlayer (Fig. 6i, Bohrmann et al., 2019). While all other classes identify quite clearly with their vp/resistivity combination, this carbonate class is mainly unique in the SGR parameter spaces (Fig. 6d, e). An indication of this non-uniqueness in the vp and resistivity space can be seen at the borders of anomaly I, where this class also occurs: without SGR information the carbonates would most likely be identified as low concentration of gas hydrates which stresses the importance of additional stratigraphic information. The addition of further classes results in a spectrum of four classes for the carbonates which does not enhance our knowledge from the observations (4th row in Fig. 5b). The second anomaly, starting at 98 mbsf, remains completely stable (100 %) and covers the suspected higher gas hydrate concentrations. This class distinctively detaches from others by high vp/high resistivity characteristics (Fig. 6c) and is not dependent on SGR information but consistent with the interpretation of gas hydrates. The last class remains at 98 % very stable and covers homogeneous background clay in depths of 0–15 mbsf and 40–80 mbsf. While the increase in velocity of the upper part indicates the compaction trend, the general characteristics of its distribution are low vp, low resistivity, and low SGR signals. The stability of this class is the most valuable information to us since it defines the depth section suitable to calibrate our model to derive the critical porosities from the background signal.

3.2. SCA-DEM model

The result of our background model calibration yields, for the elastic part of the formulation, valid critical porosities of 0.57–0.6, which are at the high end of the allowed range (Fig. 7). Critical porosities for the electric part are lower and range between 0.3 and 0.4. From the valid value triplets with deviation errors below 3 % between the derived elastic and electric properties, we require porosities of 70 % at the upper part of the borehole and 50–60 % in the lower part (Fig. 8c). A small but systematic increase in porosity with depth between 45 and 80 mbsf is supported by the fact that we observe a decrease in vp and an increase in conductivity at this depth range. A reason for this unusual behavior may be found lateral variations of the seep structure. For the identified anomalies I and II, the resulting concentrations are very prominent. Due to the varying porosity with depth and the probability-driven value range, we present and refer to the gas hydrate and free gas content as the percentage of the total volume (concentration/content) rather than pore space specific saturation levels (Fig. 8d, e). The first anomaly contains hydrate concentrations between 10 and 20 % while the second anomaly reaches around 30 % (Fig. 8d). Free gas concentrations reach around 1 % for both anomalies (Fig. 8e). The free gas concentration in the first anomaly is large enough in relation to the gas hydrate concentration to cancel the expected increase in vp completely while producing a large anomaly in the conductivity signal. However, we observe that also the second anomaly requires an equal gas concentration to fit both, the vp and conductivity, signals. Most of the background data indicate very low hydrate concentrations of ≤2 % and very low gas concentrations of ≤0.25 %. Since the background model is calibrated to fit the background signal for 0 % hydrate and 0 % free gas, these deviations may be attributed to the error floor in the forward calculations. An exception yields the signal of authigenic carbonates at depths between 85 and 98

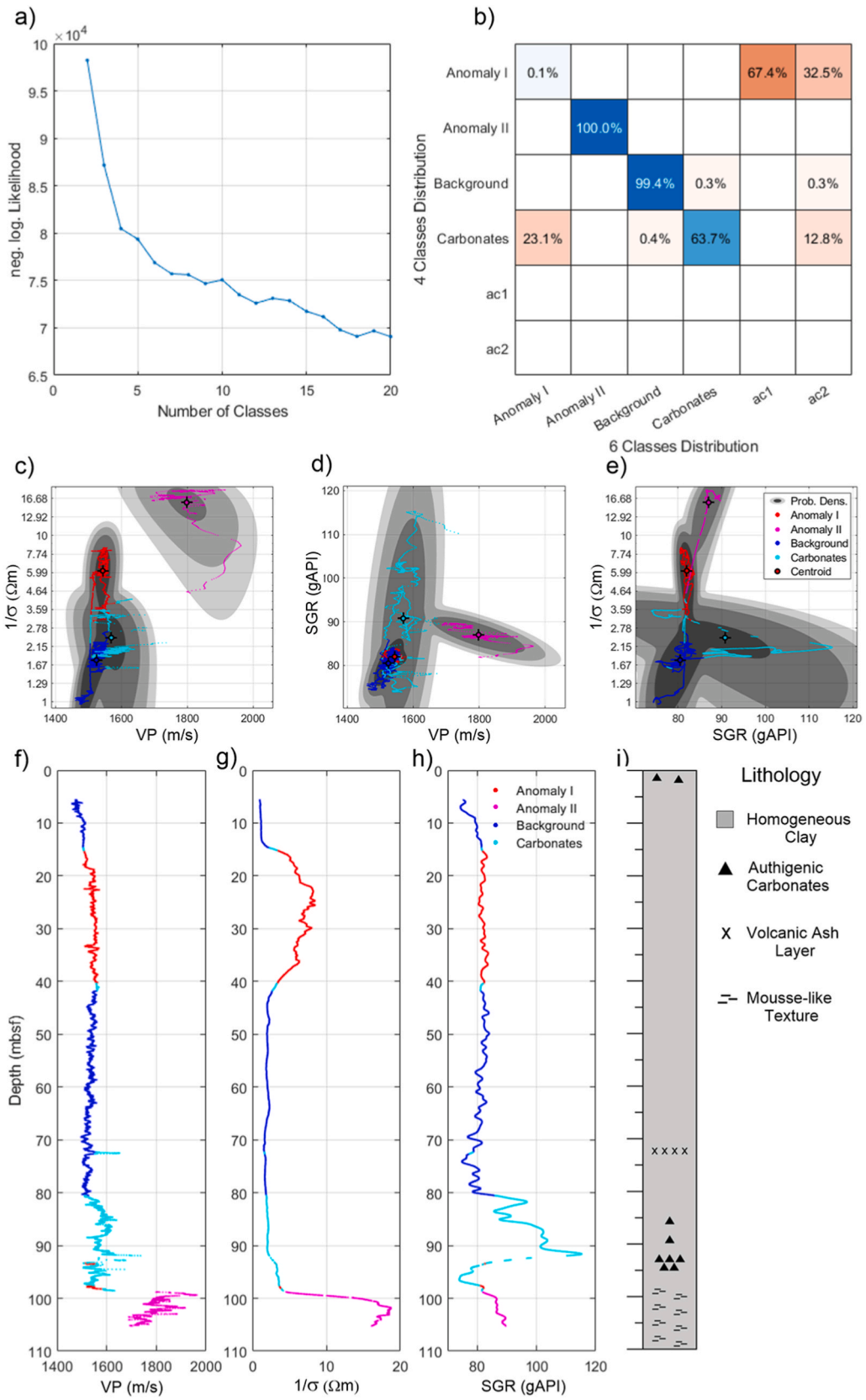

Fig. 6. Results of classification of vp, resistivity (1/conductivity) and SGR data by Gaussian Mixture Modeling. (a) Elbow Method results for an increasing number of classes, indicating an optimum at 4–6 classes. (b) Pseudo confusion matrix showcasing the effect of an increase from four initial classes to six classes (ac1, ac2). (c–e) Distribution of four data clusters is shown in parameter cross plots between velocity, resistivity, and spectral gamma ray. (f–h) Final classification of the borehole data as depth sections. (i) Lithological sequence identified on core data after Bohrmann et al. (2019).

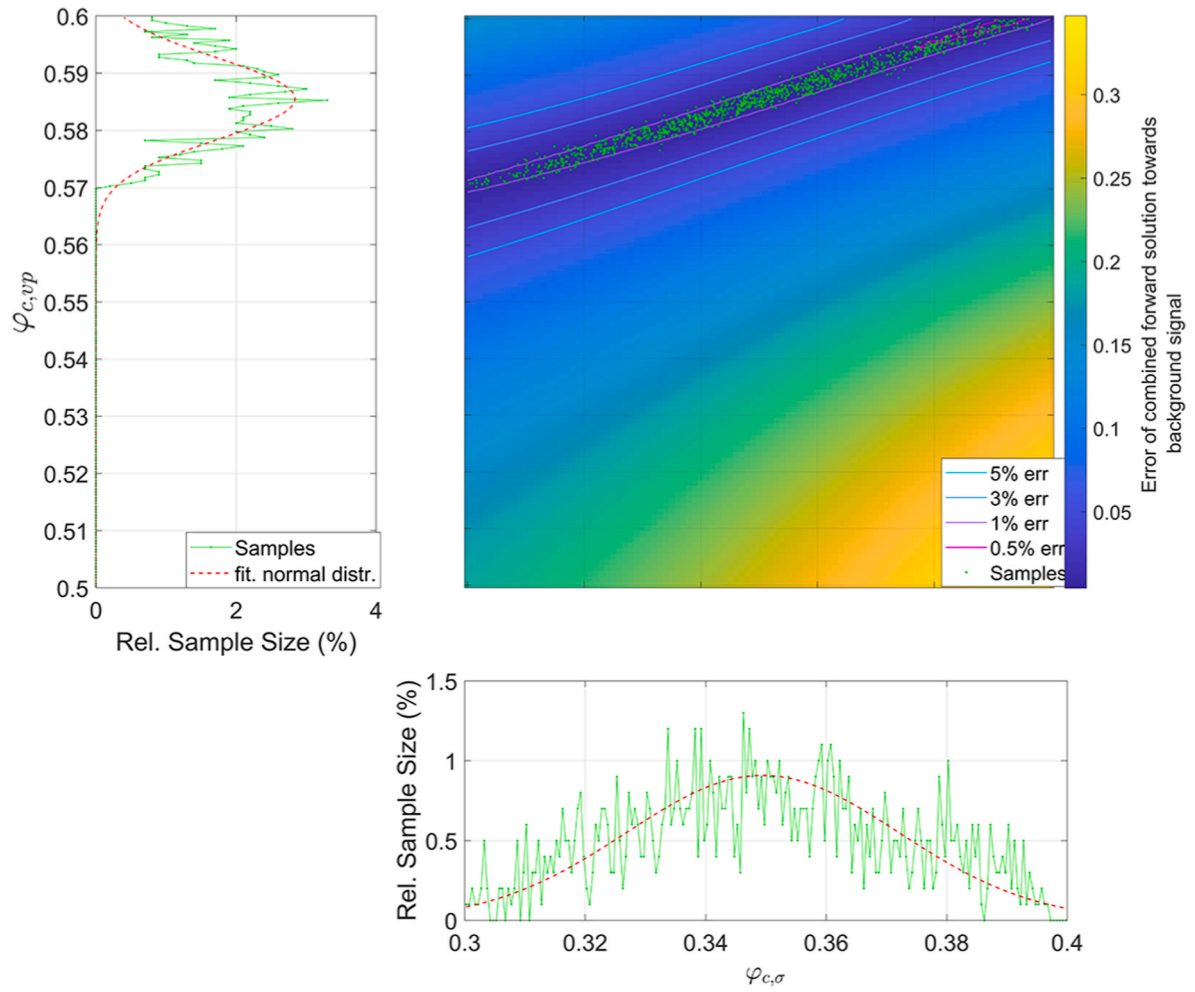

Fig. 7. Valid critical porosity pairs for the electric ($\varphi_{c,vp}$) and elastic part ($\varphi_{c,vp}$) are shown as sample distribution in the lower and left part, and the corresponding cross plot in the upper right. The values are calculated on basis of the identified background host medium by the Gaussian Mixture Models (background model calibration in Fig. 3 and fall below the error threshold, indicated by error boundaries. The porosity is determined from these values which are used to invert for the gas hydrate/free gas concentrations.

mbsf: since we did not implement the carbonate class of the GMM in the background model, the algorithm produces a false, smaller hydrate concentration of ≤5 % with 0.5 % free gas for this area. This is also true for anomaly II where a slight increase in SGR indicates a corresponding elevated carbonate content (Bohrmann et al., 2023).

4. Discussion

4.1. Method evaluation

Our new joint methodology of combining p-wave velocity and conductivity information can quantify free gas/gas hydrate mixtures. The ability to distinguish both phases relates to the combination of complementary sensitivities of elastic and electric methods while avoiding disparities often found when comparing single elastic with single electric methods.

A combination of empirical models can be applicable for certain cases but the high clay content encountered in this borehole favors the incorporation of a conductive matrix by the SCA-DEM model. A good constraint on changes in the background formation is highly important and can be achieved by GMM for which SGR information serve as a stratigraphic indicator for the elastic and electric measurements. For remotely sensed geophysical datasets that commonly lack similar information, a stratigraphic interpretation can serve this purpose. Unidentified or neglected formation changes rapidly lead to wrong results as shown for the carbonate occurrences in the lower part of the borehole. The forward calculation from rock physics to geophysical parameters theoretically requires a precise set of parameters for each constituent in each formation to be fully determined, which we do not have. Our data-driven approach hereby reflects the limitations in knowledge of the formation properties and the geometrical properties of the constituents. Fixing the aspect ratio of all constituents to the same value may not be realistic, but yields the ability to use critical porosities as a calibration method for our model, at least for the most common background medium. Theoretically, an iteration of all SCA-DEM-based parameters in a completely statistical approach would be even more beneficial at this point but impossible to solve in practice based on the sheer amount of data and calculations required. While the stacking sequence of the SCA-DEM model influences the result, a change from pore space occupying to matrix supporting hydrate would rather increase the hydrate concentration to explain our data which is less compatible with the values derived from the independent chloride analysis. For both anomalies, the retrieved concentrations for gas hydrate do not fully match the calculated hydrate content from pore water chloride measurements, which scatter in a lower range from 0-10 % and 10–20 % of the bulk volume respectively. This equals to around 5–10 % average deviation from the retrieved concentration of the highest probability for both anomalies, while generally valid solutions within the 95 % confidence interval can be found partially coinciding or within small deviations (Fig. 8d). A rather small percentage of hydrate concentration in anomaly II can

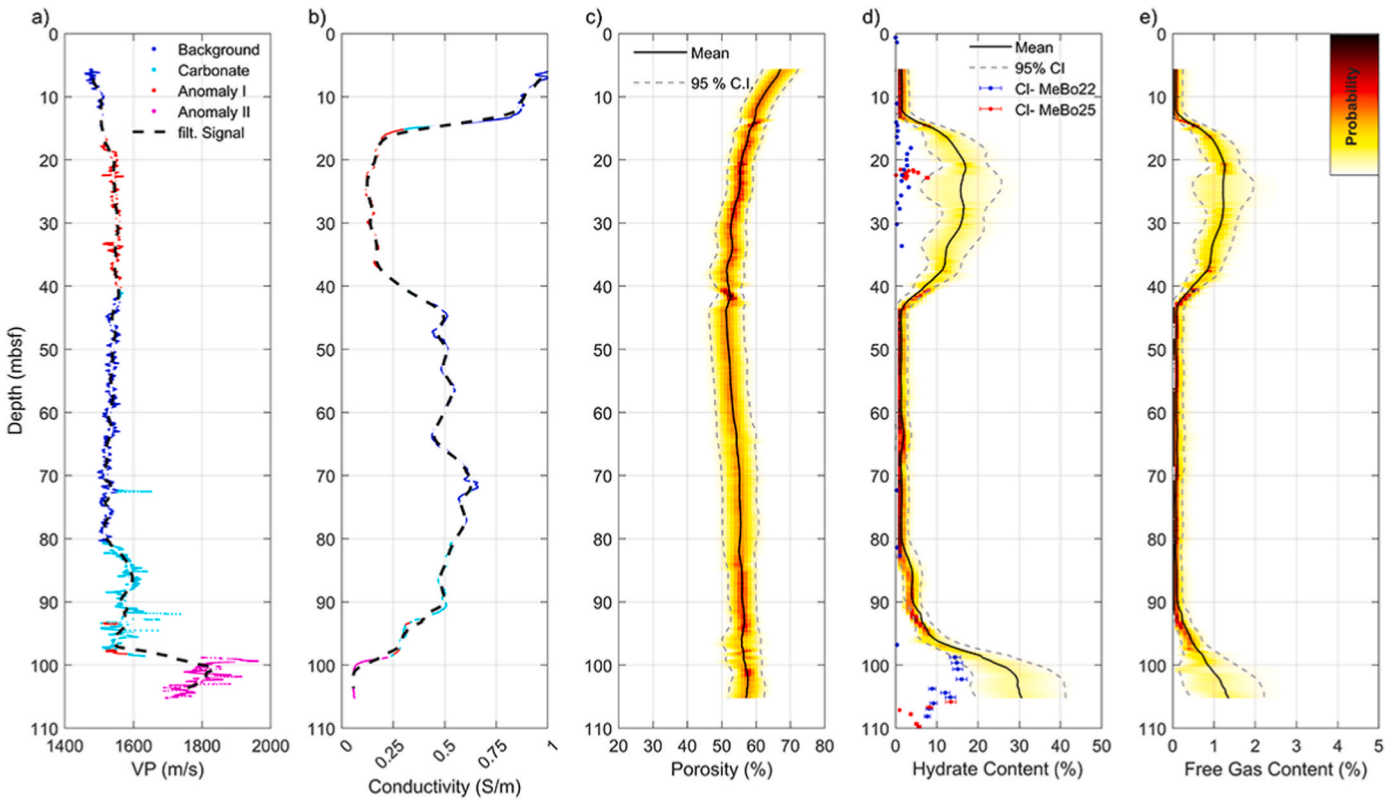

Fig. 8. Final results from full inversion. Observed and filtered p-wave velocity (a) and conductivity (b). Color coding shows the GMM classifications (see Fig. 6). (c) porosity distribution identified by background model calibration. Gas hydrate (d) and gas (e) concentrations identified by SCA-DEM full model inversion. Note that we present the results as total hydrate and free gas content rather than pore space saturation. The modeling results are shown as probability density distributions by color coding with means and 95 % confidence intervals. Also shown in (d) are independent hydrate concentrations based on porewater (Cl^-) samples with error bars scaled to the confidence interval of the porosity.

actually be attributed to a small increase in carbonate content, identified by Bohrmann et al. (2023). In comparison to the retrieved hydrate saturation for the larger occurrence of carbonates above, this should have only a very small effect. We attribute the remaining mismatch to the fact, that vp measurements, conductivity measurements, and sample analysis do not observe hydrate distribution on the same spatial scale: the greater depths of investigation but lower resolutions of the MAT and DI tool may not resolve the heterogeneity of the seep structure at the drill site while sampling only provides very local insights. This adds to the fact of two closely drilled boreholes that are still separated by 5 m promoting a probable scenario where higher concentrations are found further away from the MAT probe in one borehole but well within range of the dual induction probe in the second borehole. This is consistent with slightly higher hydrate concentrations from chloride sampling for MeBo 25 in the upper anomaly (Fig. 8d). Furthermore, the closer proximity to MeBo 26 with its heavy gas release while drilling suggests a higher potential for hydrate formation in this direction. In this case, the shallower anomaly would be more local or patchy while the lower anomaly can be thought of as a more laterally consistent feature.

4.2. Geological implications

Another possible explanation for the deviations may be the effect of lateral variability of the gas hydrate system on the anisotropy of physical properties. Even though we decided to implement hydrate as pore-filling in our model, thin veins or lenses as grain displacing configuration are described as possible occurring type of hydrate for marine, fine-grained sediments (Holland et al., 2008). Dual induction probes are sensitive to anisotropic behavior caused by hydrate-filled fractures and veins (Cook et al., 2014). Inclined to near-vertical, hydrate-filled fractures cross-cutting the horizontally stratified clay sequences may function as a resistive barrier towards the horizontal eddy currents induced by the horizontal coaxial coils of the probe: a characteristic that amplifies the observed electrical resistivity. Low-concentrated hydrate being formed outside of the primary porosity in the matrix of fine-grained clay on the other hand does not necessarily increase seismic velocity (Cook et al., 2010). Since the elastic formulation of SCA-DEM is able to derive s-wave velocity, the inversion for this parameter, if available, could provide valuable, additional information for these cases (Siriam et al., 2014; Haines et al., 2022). Very discrete features like hydrates in veins and cracks contradict the idea of a homogenous, representative effective medium model and cannot be generated with our SCA-DEM model. However, for hydrate in a matrix-supporting configuration, our joint SCA-DEM modeling suggests an increase in vp and resistivity even for lower amounts of hydrate. In this case, the applied effective medium model would not be suited to represent this scenario satisfactorily. Vertical fracture networks at the Formosa Ridge seep site have been identified by seismic attributes and linked to hydraulic fracturing due to accumulated free gas concentrations beneath the BGHS by Kunath et al. (2022). This is mostly the case for the chimney beneath the lower carbonates at 90 mbsf, but also for some intervals higher up in the stratigraphy. Given the active fluid and gas seeps, there is a high probability of existing fracture networks in the upper anomaly directly below the seep site. This modern fracture network is unlikely to be clogged up by hydrates completely even if other migration pathways formed outside of this network (Hsu et al., 2018). The results of Bohrmann et al. (2019) and Kunath et al. (2022) rule out larger volumes of hydrate in the borehole. Generally, the endothermic dissociation of hydrate leads to a self-preservation process of larger hydrate accumulations by forming water-ice covers when being brought up out of the GHSZ aboard the

research vessel. Still, no actual hydrates are found in the core samples, only soupy or mousse-like clay-water mixtures for given depth intervals in agreement with the concentrations we derive from the chloride sampling. Thus Bohrmann et al. (2019) infer that the initial occurrence of hydrates in the borehole may only be distributed by smaller, disseminated hydrate grains. While this generally supports the idea of low amounts of hydrate being detected by the induction probe but not by the MAT probe for the upper anomaly, it contradicts the differences that are observed between both anomalies: low amounts of hydrate in thin veins should have less effect on the induction probe than high amounts of hydrate in larger veins. Instead, we observe a large conductivity anomaly in both cases but only the distinct velocity anomaly in the lower part. This suggests that the geophysical signatures must relate to concentration variations, since fracture networks are present for both anomalies, most probably being actively used by fluids and gas expulsions.

5. Conclusions

Joint electric and elastic data analysis allows us to distinguish between solid hydrate and free gas content, even if they occur simultaneously within the GHSZ. If no free gas is present, the combination of complementary sensitivities is a robust way to eliminate the uncertainties of the single methods. A key factor is the correct identification and delineation of the background signals from anomalies which we use to build up a background model and determine the porosity. Through our presented probabilistic approach, we offer a method to determine the uncertainties in the results, produced by ambiguous solutions for gas hydrate/free gas mixtures. Our findings match the results from recovered cores and interpretation of the seep site by other authors and suggest a low hydrate content of 10–20 % for the upper anomaly and a higher concentration of gas hydrates (around 30 %) for the lower part, both with an equally low amount (1 %) of free gas. Still, we find deviations between our results and values derived by chloride concentration, but moreover, we have to consider the fact that the upper anomaly is not indicated by the vp data at all. Both factors can be related to inconsistent spatial resolutions between methods but also the heterogeneity of the seep structure and the occurrence of gas hydrates as disseminated grains vs. solid veins as geological implications. From previously made observations we can infer that vertical pathways have been identified for the seep structure. Thus, the absence of a vp anomaly in the upper part is either prevented by the unique combination of hydrate and free gas concentration in the upper anomaly or by a resolution issue. The identified free gas concentration is most likely related to trapped, residual gas from the overpressure-driven opening and closure of the fracture network, which is thought to occur periodically. By the presentation of our approach on a commonly used borehole dataset that is representative for a variety of existing datasets, we showcase our workflow from scratch to jointly integrate data and invert for gas hydrate and free gas concentration simultaneously. The effort, especially for the delineation of the background model, hereby scales with the expected, geologic complexity. The limitations we met are not unique to our approach but mostly based on uncertainties and assumptions that are required for remote sensing and in marine environments. The application on geophysical datasets is therefore the next consequential step. While the determination of the given gas hydrate and free gas concentration by a joint parameter combination is a more robust approach than traditional schemes, the incorporation of additional information may improve the methodology. The elastic formulation of SCA-DEM is capable to derive and invert for s-wave velocity which may improve hydrate estimates in a three-dimensional approach.

Funding

The cruise was financed in Germany by the Ministry of Education and Science, project 660 TaiDrill – SO266 (Ref. #03G0288A). The project was funded in Taiwan by the Ministry of Science and Technology (MoST) Project TaiGer drill (MOST107-3113-M-002-004, NSTC111-2611-M-001-009).

Open research

The borehole p-wave velocity, electrical resistivity, chloride and spectral gamma ray data used in the study are available at PANGEA (see references).

Version 2021b of MATLAB used for all modeling and data analysis is commercially available at http://mathworks.com.

RPH Tools for Matlab was used for the elastic formulation of the SCA-DEM model and is available from https://pangea.stanford.edu/departments/geophysics/dropbox/SRB/public/data/RPHtools.htm.

The developed MATLAB script set for the elastic/electric formulation of the SCA-DEM model will be stored on GitHub, available from https://github.com/k-reeck/SCA-DEM.

Version 3.3 of the Seawater Library for MATLAB by CSIRO and Morgan P. P. (1994) was used to correct the electrical conductivity of the porewater for the temperature gradient, available from https://researchdata.edu.au/csiro-marine-research-library-2006/692093.

Declaration of competing interest

The authors declare that they have no known competing financial interests or personal relationships that could have appeared to influence the work reported in this paper.

Data availability

Data and code is available from the listed repositories.

Acknowledgments

We are grateful to the master of the vessel, Lutz Mallon and his crew, and the shipping operator Briese Schiffahrt GmbH & Co KG for continuous support. We further like to thank Prof. Dr. Tongcheng Han for providing test values to help with the verification of our SCA-DEM code. We appreciate and would like to thank the reviewers who provided insightful comments to help us improve the manuscript.

References

Archie, G.E., 1942. The electrical resistivity log as an aid to determining some reservoir characteristics. Transactions of the American Institute of Mining and Metallurgical Engineers 146, 54–62 doi:10.2118%2F942054-g.

Attias, E., Amalokwu, K., Watts, M., Falcon-Suarez, I.H., North, L., Hu, G.W., Best, A.I., Weitemeyer, K., Minshull, T.A., 2020. Gas hydrate quantification at a pockmark offshore Norway from joint eective medium modeling of resistivity and seismic velocity ff. Mar. Petrol. Geol. 113 https://doi.org/10.1016/j.marpetgeo.2019.104151.

Berndt, C., Crutchley, G., Klaucke, I., Jegen, M., Lebas, E., Muff, S., Lieser, K., Roth, T., Chi, W.-C., Feseker, T., 2014. Geological Controls on the Gas Hydrate System of Formosa Ridge, South China Sea, OCEANS 2014 – TAIPEI. https://doi.org/10.1109/OCEANS-TAIPEI.2014.6964481.

Berndt, C., Chi, W.-C., Jegen, M., Lebas, E., Crutchley, G., Muff, S., Hölz, S., Sommer, M., Lin, S., Lisa, C.-S., Lin, A.T., Klaeschen, D., Klaucke, I., Chen, L., Hsu, H.-H., Kunath, P., Elger, J., McIntosh, K.D., Fesker, T., 2019. Tectonic controls on gas hydrate distribution off SW Taiwan. J. Geophys. Res. Solid Earth 124, 1164–1184. https://doi.org/10.1029/2018JB016213.

Berryman, J.G., 1980. Long-wavelength propagation in composite elastic media. J. Acoust. Soc. Am. 68, 1809–1831. https://doi.org/10.1121/1.385172.

Berryman, J.G., 1995. Mixture theories for rock properties. In: Ahrens, T.J. (Ed.), Rock Physics and Phase Relations: a Handbook of Physical Constants. American Geophysical Union, Washington DC, pp. 205–228. https://doi.org/10.1029/RF003p0205.

Bohrmann, G., Torres, M.E., 2006. Gas hydrates in marine sediments. In: Schulz, H.D., Zabel, M. (Eds.), Marine Geochemistry. Springer, Berlin, Heidelberg. https://doi.org/10.1007/3-540-32144-6_14.

Bohrmann, G., Greinert, J., Suess, E., Torres, M., 1998. 1998. Authigenic carbonates from the Cascadia subduction zone and their relation to gas hydrate stability. Geology 26

(7), 647–650. https://doi.org/10.1130/0091-7613(1998)026<0647:ACFTCS>2.3.CO;2.
Bohrmann, G., Ahrlich, F., Bergenthal, M., Berndt, C., Chen, J., Chen, S., Chen, T., Chen, W., Chi, W., Deusner, Ch, Elger, J., Freudenthal, T., Fröhlich, S., Klein, T., Kramer, L., Kuhnert, M., Fan, L., Hsu, H., Lai, M., Yu, P., 2019. MeBo200 Methane Hydrate Drillings Southwest of Taiwan – TaiDrill Cruise No. SO266/1, 15 October – 18 November 2018, Kaohsiung (Taiwan) – Kaohsiung (Taiwan), SONNE-Berichte. https://doi.org/10.48433/cr_so266_1.
Bohrmann, G., Berndt, C., Lin, S., Tu, T.-H., Lin, A.T., Hsu, H.-H., Lai, M.-L., Chi, W.-C., Deusner, C., Elger, J., Wallmann, K., Freudenthal, T., Mau, S., Pape, T., Tseng, Y.-T., Yu, P.-S., Fan, L.-F., Chen, J.-N., Chen, S.-C., Wei, K.-Y., 2023. Geological controls on the distribution of gas hydrates in the shallow parts of the gas hydrate stability zone – constraints from seafloor drilling off Taiwan. Mar. Petrol. Geol. https://doi.org/10.1016/j.marpetgeo.2023.106253.
Bünz, S., Mienert, J., 2004. Acoustic imaging of gas hydrate and free gas at the Storegga Slide. J. Geophys. Res. C Oceans Atmos. 109, B04102 https://doi.org/10.1029/2003JB002863.
Cleary, M.P., Lee, S.-M., Chen, I.-W., 1980. Self-consistent techniques for heterogeneous media. J. Eng. Mech. Div. 106 (5), 861–887. https://doi.org/10.1061/JMCEA3.0002643.
Collett, T.S., Ladd, J., 2000. Detection of gas hydrate with downhole logs and assessment of gas hydrate concentrations (saturations) and gas volumes on the Blake Ridge with electrical resistivity log data. In: Paull, C.K., Matsumoto, R., Wallace, P.J., Dillon, W. P. (Eds.), Proc. ODP, Sci. Results, vol. 164. Ocean Drilling Program), College Station, TX, pp. 179–191. https://doi.org/10.2973/odp.proc.sr.164.219.2000.
Constable, S., Lu, R., Stern, L.A., Du Frane, W.L., Roberts, J.J., 2020. Laboratory electrical conductivity of marine gas hydrate. Geophys. Res. Lett. 47, e2020GL087645 https://doi.org/10.1029/2020GL087645.
Cook, A.E., Barbara, I., Anderson, B.I., Malinverno, A., Mrozewski, S., Goldberg, D.S., 2010. Electrical anisotropy due to gas hydrate-filled fractures. Geophysics 75 (6), F173–F185. https://doi.org/10.1190/1.3506530.
Cook, A.E., Goldberg, D.S., Malinverno, A., 2014. Natural gas hydrates occupying fractures: A focus on non-vent sites on the Indian continental margin and the northern Gulf of Mexico, Marine and Petroleum Geology. https://doi.org/10.1016/j.marpetgeo.2014.04.013.
CSIRO, Morgan, P.P., 1994. SEAWATER: A Library of MATLAB Computational Routines for the Properties of Seawater, 3.3 (Software). https://researchdata.edu.au/csiro-marine-research-library-2006/692093.
Deisenroth, M.P., Faisal, A.A., Ong, C.S., 2020. Mathematics for Machine Learning. Cambridge University Press, Cambridge. https://doi.org/10.1017/9781108679930.
Dickens, G.R., 2003. Rethinking the global carbon cycle with a large, dynamic and microbially mediated gas hydrate capacitor. Earth Planet Sci. Lett. 213 (Issues 3–4), 169–183. https://doi.org/10.1016/S0012-821X(03)00325-X.
Dvorkin, J., Nur, A., 1996. Elasticity of high-porosity sandstones: theory for two North Sea data sets. Geophysics 61 (5), 1363–1370. https://doi.org/10.1190/1.1444059.
Edwards, R.N., 1997. On the resource evaluation of marine gas hydrate deposits using sea-floor transient electric dipole-dipole methods. Geophysics 62 (1), 63–74. https://doi.org/10.1190/1.1444146.
Ellis, M.H., 2008. Joint Seismic and Electrical Measurements of Gas Hydrates in Continental Margin Sediments. University of Southampton, School of Ocean and Earth Science, Doctoral Thesis, p. 284pp.
Ellis, D.V., Singer, J.M., 2007. Well Logging for Earth Scientists, second ed. Springer, Berlin. https://doi.org/10.1007/978-1-4020-4602-5.
Feng, D., Chen, D., 2015. Authigenic carbonates from an active cold seep of the northern South China Sea: new insights into fluid sources and past seepage activity. Deep Sea Res. Part II Top. Stud. Oceanogr. 122, 74–83. https://doi.org/10.1016/j.dsr2.2015.02.003.
Freudenthal, T., 2020a. Spectrum Gamma Ray Borehole Logging Data of MeBo Sediment Core GeoB23213-1. PANGAEA (Dataset). https://doi.org/10.1594/PANGAEA.914594.
Freudenthal, T., 2020b. Spectrum Gamma Ray Borehole Logging Data of MeBo Sediment Core GeoB23227-1. PANGAEA (Dataset). https://doi.org/10.1594/PANGAEA.914595.
Freudenthal, T., 2020c. Acoustic Borehole Logging of MeBo Sediment Core GeoB23213-1. PANGAEA (Dataset). https://doi.org/10.1594/PANGAEA.914616.
Freudenthal, T., 2020d. Resistivity RDeep and RMedium Borehole Logging Data of MeBo Sediment Core GeoB23227-1. PANGAEA (Dataset). https://doi.org/10.1594/PANGAEA.914584.
Freudenthal, T., Wefer, G., 2013. Drilling core on the sea floor with the remote-controlled sea floor drilling rig MeBo, Geosci. Instrum. Method. Data Syst 2, 329–337. https://doi.org/10.5194/gi-2-329-2013.
Glover, P., Hole, M., Pous, J., 2000. A modified Archie's Law for two conducting phases. Earth Planet Sci. Lett. 180, 369–383. https://doi.org/10.1016/S0012-821X(00)00168-0.
Grevemeyer, I., Villinger, H., 2000. Gas hydrate stability and the assessment of heat flow through continental margins. Geophys. J. Int. 145 (3), 647–660. https://doi.org/10.1046/j.0956-540x.2001.01404.x.
Haines, S.S., Collett, T.S., Yoneda, J., Shimoda, N., Boswell, R., Okinaka, N., 2022. Gas hydrate saturation estimates, gas hydrate occurrence, and reservoir characteristics based on well log data from the hydrate-01 stratigraphic test well, Alaska north slope. Energy Fuels 36 (6), 3040–3050. https://doi.org/10.1021/acs.energyfuels.1c04100.
Han, T., Best, A.I., MacGregor, L.M., Minshull, T.A., 2011. Joint elastic-electrical effective medium models of reservoir sandstones. Geophys. Prospect. 59 (4), 777–786. https://doi.org/10.1111/j.1365-2478.2011.00956.x.
Helgerud, M.B., Dvorkin, J., Nur, A., 1999. Elastic-wave velocity in marine sediments with gas hydrates: effective medium modeling. Geophys. Res. Lett. 26 (13), 2021–2024. https://doi.org/10.1029/1999GL900421.
Holland, M., Schultheiss, P., Roberts, J., Druce, M., 2008. Observed gas hydrate morphologies in marine sediments. In: Proceedings of the 6th International Conference on Gas Hydrates (ICGH 2008), Vancouver British Columbia, Canada, July 6-10, 2008.
Hornby, B.E., Schwartz, L.M., Hudson, J.A., 1994. Anisotropic effective-medium modeling of the elastic properties of shales. Geophysics 59 (10), 1570–1583. https://doi.org/10.1190/1.1443546.
Hsu, H.-H., Liu, C.-S., Morita, S., Tu, S.-L., Lin, S., Machiyama, H., Azuma, W., Ku, C.-Y., Chen, S.-C., 2018. Seismic imaging of the Formosa Ridge cold seep site offshore of southwestern Taiwan. Mar. Geophys. Res. 39, 523–535. https://doi.org/10.1007/s11001-017-9339-y.
Jackson, P.D., Smith, D.T., Stanford, P.N., 1978. Resistivity-porosity-particle shape relationships for marine sands. Geophysics 43 (6), 1250–1268. https://doi.org/10.1190/1.1440891.
Kumar, P., Collett, T.S., Boswell, R., Cochran, J.R., Lall, M., Mazumdar, A., Ramana, M. V., Ramprasad, T., Riedel, M., Sain, K., Sathe, A.V., Vishwanath, K., Yadav, U.S., 2014. Geologic implications of gas hydrates in the offshore of India: krishna–godavari basin, mahanadi basin, andaman sea, Kerala–konkan basin. Mar. Petrol. Geol. 58, 29–98. https://doi.org/10.1016/j.marpetgeo.2014.07.031.
Kunath, P., Crutchley, G., Chi, W., Berndt, C., Liu, C., Elger, J., Klaeschen, D., Bohrmann, G., 2022. Episodic venting of a submarine gas seep on geological time scales: Formosa Ridge, northern South China sea. J. Geophys. Res. Solid Earth 127. https://doi.org/10.1029/2022jb024668.
Kvenvolden, K., McMenamin, M., 1980. Hydrates of Natural Gas: A Review of Their Geologic Occurrence. USGS Circular. https://doi.org/10.3133/cir825.
Lee, M.W., Collett, T.S., 2005. Controls on the Physical Properties of Gas-Hydrate-Bearing Sediments Because of the Interaction Between Gas Hydrate and Porous Media. USGS Scientific Investigations Report 2005-5143. https://doi.org/10.3133/sir20055143.
Lee, M.W., Hutchinson, D.R., Collett, T.S., Dillon, W.P., 1996. Seismic velocities for hydrate-bearing sediments using weighted equation. J. Geophys. Res. 101 (B9), 20347–20358. https://doi.org/10.1029/96JB01886.
Lin, S., Bohrmann, G., 2022. Chloride concentrations and calculated gas hydrate saturations in sediments collected at Formosa Ridge, RV Sonne cruise SO266/1. https://doi.org/10.1594/PANGAEA.953067. South China Sea.
MATLAB, 2021, version 9.11.0 (R2021b), Natick, Massachusetts: The MathWorks Inc. (Software).
Mavko, G., Mukerji, T., Dvorkin, J., 2009. The Rock Physics Handbook: Tools for Seismic Analysis of Porous Media, second ed. Cambridge University Press, Cambridge. https://doi.org/10.1017/CBO9780511626753.
Mukerji, T., 2009. RPHtools Matlab Scripts (Software). https://pangea.stanford.edu/research/srb/books/RPHII/RPHtools/.
Pan, H.J., Zhang, Y., Swidinsky, A., Li, H.B., 2017. Joint Stochastic Inversion of Elastic-Electrical Data for Reservoir Parameters of Gas Hydrate Bearing Sediment. In: 79th EAGE Conference & Exhibition 2017, vol. 2017, pp. 1–5. https://doi.org/10.3997/2214-4609.201701046. Paris , France, 12-15 June 2017.
Pan, H., Hongbing, L., Jingyi, C., Riedel, M., Holland, M., Zhang, Y., Shengjuan, C., 2020. Quantification of gas hydrate saturation and morphology based on a generalized effective medium model. Mar. Petrol. Geol. 113 https://doi.org/10.1016/j.marpetgeo.2019.104166.
Panday, L., Sain, K., 2022. Joint inversion of resistivity and sonic logs using gradient descent method for gas hydrate saturation in the Krishna Godvari offshore basin, India. Mar. Geophys. Res. 43, 29. https://doi.org/10.1007/s11001-022-09491-z.
Peckmann, J., Reimer, A., Luth, U., Luth, C., Hansen, B.T., Heinicke, C., Hoefs, J., Reitner, J., 2001. Methane-derived carbonates and authigenic pyrite from the northwestern Black Sea. Mar. Geol. 177 (1–2), 129–150. https://doi.org/10.1016/S0025-3227(01)00128-1.
Qin, X.-W., Lu, J., Lu, H.-L., Qiu, H.-J., Liang, J.-Q., Kang, D.-J., Zhan, L.-S., Lu, H.-F., Kuang, Z.-G., 2020. Coexistence of natural gas hydrate, free gas and water in the gas hydrate system in the Shenhu Area, South China Sea. China Geology 3, 210–220. https://doi.org/10.31035/cg2020038.
Ruppel, C.D., Waite, W.F., 2020. Timescales and processes of methane hydrate formation and breakdown, with application to geologic systems. J. Geophys. Res. Solid Earth 125. https://doi.org/10.1029/2018JB016459.
Sheng, P., 1990. Effective-medium theory of sedimentary rocks. Phys. Rev. B 41 (7), 4507–4512. https://doi.org/10.1103/PhysRevB.41.4507.
Sheng, P., 1991. Consistent modeling of the electrical and elastic properties of sedimentary rocks. Geophysics 56, 1236–1243. https://doi.org/10.1190/1.1443143.
Siriam, G., Dewangan, P., Ramprasad, T., 2014. Modified effective medium model for gas hydrate bearing, clay-dominated sediments in the Kirshna-Godavari Basin. Mar. Petrol. Geol. 58, 321–330. https://doi.org/10.1016/j.marpetgeo.2014.01.005.
Sloan, E.D., 1998. Physical/chemical properties of gas hydrates and application to world margin stability and climatic change. Geol. Soc. Lond., Special Publ. 137, 31–50. https://doi.org/10.1144/GSL.SP.1998.137.01.03.
Ussler III, W., Paull, C.K., 2001. Ion exclusion associated with marine gas hydrate deposits. In: Paull, C.K., Dillon, W.P. (Eds.), Natural Gas Hydrates: Occurrence, Distribution, and Detection. https://doi.org/10.1029/GM124p0041.
Waite, W.F., Spangenberg, E.K., 2013. Gas hydrate formation rates from dissolved-phase methane in porous laboratory specimens. Geophys. Res. Lett. 40, 4310–4315. https://doi.org/10.1002/grl.50809.
Westbrook, G.K., Carson, B., Musgrave, R.J., Suess, E., 1994. Proceedings of the Ocean Drilling Program, ume 146. Ocean Drilling Program, College Station, Texas, p. 477. Initial Reports.

Wood, A.B., 1941. A Textbook of Sound, second ed. MacMillan, New York.
Wu, N., Zhang, H., Yang, S., Zhang, G., Liang, J., Lu, J., Su, X., Schultheiss, P., Holland, M., Zhu, Y., 2011. Gas hydrate system of Shenhu area, northern South China sea, geochemical results. J. Geol. Res. 2011 https://doi.org/10.1155/2011/370298.
Wyllie, M.R.J., Gregory, A.R., Gardner, L.W., 1956. Elastic wave velocities in heterogeneous and porous media. Geophysics 21 (No. 1), 41–70. https://doi.org/10.1190/1.1438217.
Zhang, H., Yang, S., Wu, N., Su, X., Holland, M., Schultheiss, P., Rose, K., Butler, H., Humphrey, G., GMGS-1 Science Team, 2007. 2007. Successful and surprising results for China's first gas hydrate drilling expedition. In: Fire in the Ice. US DOE–NETL newsletter) Fall, pp. 6–9.